Sustainable wearable infrared shielding bamboo fiber fabrics loaded with antimony doped tin oxide/silver binary nanoparticles

Xin-Yao Ye[1,2] · Yu Chen[1,2] · Jing Yang[2] · Hai-Yan Yang[2] · Da-Wei Wang[2] · Ben Bin Xu[3] · Junna Ren[3,4] · Deepak Sridhar[5] · Zhanhu Guo[3*] · Zheng-Jun Shi[1,2*]

[1] *Key Laboratory for Forest Resources Conservation and Utilization in the Southwest Mountains of China, Ministry of Education, Southwest Forestry University, Kunming 650224, China*

[2] *Key Laboratory of State Forestry and Grassland Administration on Highly-Efficient Utilization of Forestry Biomass Resources in Southwest China, Southwest Forestry University, Kunming, 650224, China*

[3] *Integrated Composites Lab, Department of Mechanical and Construction Engineering, Northumbria University, Newcastle Upon Tyne, NE1 8ST, UK*

[4] *College of Materials Science and Engineering, Taiyuan University of Science and Technology, Taiyuan, 030024, China*

[5] *Zentek Ltd. 24 Corporate Crt, Guelph, Ontario, N1G 5G5 Canada*

* *Corresponding authors*

E-mail address: shizhengjun1979@163.com (Z.J. Shi); zhanhu.guo@northumbria.ac.uk (Z. Guo)

Abstract

The development of modern infrared detection technology has increased the possibility that military targets will be identified. Therefore, the task of protecting these targets is urgent extremely. The stealth materials should be versatile to achieve the performance requirements of different applications. In this study, an antimony doped tin oxide/silver/bamboo fibers (ATO-Ag-BFs) composite fabrics with multi-functional properties including infrared protection, antibacterial and hydrophobic properties were developed by the combination of ATO loading, chemical deposition and hot press process. The ATO-Ag-BFs fabrics possessed plasmon resonance absorption properties of near-infrared light, which was attributed to the formation of Schottky junction by direct contact between Ag and ATO nanoparticles. The infrared emissivity is as low as 0.68 in the 8–14 μm thermal imaging band, which allowed the target to blend well into environmental background. In addition, the n-hexadecyl mercaptan-treated ATO-Ag-BFs exhibited hydrophobic properties with a water contact angle (WCA) of 147.7°. Especially, the combination of Ag and ATO nanoparticles endowed bamboo fiber fabrics with antibacterial properties, with 100% inhibition rate against *Escherichia coli* (*E. coli*) and *Staphylococcus aureus* (*S. aureus*). The ATO-Ag-BFs can be applied in the field of wearable infrared and thermal radiation shielding to meet the requirements for concealment in harsh environments.

Keywords Bamboo fibers · Antimony doped tin oxide (ATO) · Electroless plating silver · Hydrophobic · Antibacterial · Infrared stealth

1. Introduction

Due to the progress of modern infrared detection technology, it has posed a significant threat to the concealment of military targets [1]. Hence, stealth technology has attracted worldwide attention and has become a crucial subject of conversation in the military field [2, 3]. Stealth technology refers to the technology that makes the object unrecognizable by reducing external signals (acoustic [4], radar [5], visual signals [6], and infrared [7]) used to identify objects. And specifically, infrared stealth is a technique that makes the infrared radiation emitted by an object as similar as possible to the background radiation, so that the infrared detection system cannot distinguish the military target [8, 9]. Although all objects with temperatures above –273.15 °C emit infrared radiation (0.78–1000 μm), most infrared radiation signals are absorbed and scattered by carbon dioxide molecules, water vapor, or particulates in the air. Only far-infrared (8–14 μm), mid-infrared (3–5 μm), and near-infrared (0.78–2.5 μm) signals have outstanding penetration [10]. Objects of different temperatures emit different wavelengths of infrared radiation. The infrared detection system relies on the difference in thermal radiation caused by the temperature of the target and the background to find and identify the target [11]. The intensity of infrared radiation is proportional to the fourth power of the surface temperature of an object according to the Stefan-Boltzmann law, and the infrared light shining on an object can transfer thermal energy to the object [12]. Hence, the most effective methods of concealment to avoid infrared identification and detection is to make the detectable infrared signal as similar as possible to the environmental radiation by using infrared shielding materials or decreasing the surface temperature of the infrared

emitting object [13, 14]. Therefore, using materials that can shield the infrared signal to dip-coat the object, or sealing the object with insulating materials to avoid heat diffusion to the surface of object is a feasible way to reduce the intensity of infrared radiation [15, 16]. However, for military applications, it is necessary to consider some special cases. For example, the fabric worn on the body should have antimicrobial properties to prevent wound infection when an injury occurs [17]. In harsh field environments such as swamps and jungles, waterproofing is needed to resist the harmful effects of moisture on human health. Up to now, most of the reported infrared stealth materials only have infrared stealth function [18], which is difficult to achieve the multifunctional requirements of military applications. Hence, there is a broad application prospect to develop protective clothing with multiple functions, but it is also extremely challenging.

To date, metal powders [19], conductive polymers [20], phase change materials [21], inorganic/organic composites [22], and semiconductors [23] are primary fillers or coatings used in infrared stealth fabrics. With excellent electrical conductivity, low infrared emissivity and high infrared reflectivity, metallic coatings have been a widely used as infrared stealth coating [24]. Among metal materials, Al and Ag are most used in practical applications because of their relatively low cost and excellent performance [25, 26]. However, Al inevitably has a key drawback: its infrared shielding performance deteriorates due to its tendency to oxidize when exposed to air for long periods of time. Compared with Al, Ag is not easily oxidized in air, so it is favored by researchers [27, 28]. Organic/inorganic composites and conductive polymers can be formed into various shapes because of their flexible properties. However, their mechanical properties and infrared shielding ability are poor, and the preparation process of adhesives is complicated, so their

applications are limited greatly [29]. Among them, semiconductors with a relatively wide bandgap have high reflectivity in the infrared region, and are more stable than composites and polymers in atmosphere. Therefore, like metals, they are commonly used as infrared shielding materials [10]. In recent years, the studies on infrared shielding performances of zinc oxide (ZnO), tin oxide (SnO_2), indium antimony oxide (IAO), aluminum-doped zinc oxide (AZO), indium tin oxide (ITO), and antimony tin oxide (ATO) have been reported [15, 17, 30]. Among them, ATO has been studied in detail due to its non-toxicity and low infrared emissivity, which is widely used as a substitute for ITO [31, 32]. Currently, films used for infrared and thermal radiation shielding take the form of ATO nanoparticles mixed with adhesives. Wang et al [17]. prepared a multifunctional polyacrylonitrile/AZO/Ag nanofiber membrane for infrared stealth, self-cleaning and antimicrobial applications by electrostatic spinning using a solvent thermal method and a chemical plating process. Jeong et al [10]. developed a polyurethane-antimony tin oxide fiber by electrostatic spinning, and the prepared composite fibers showed stable thermal radiation and infrared shielding properties. Unfortunately, there are few reports on the loading of ATO nanoparticles and chemical plating in the form of bio-based fibers (rather than the typical film or petroleum-based fiber form) for application in wearable infrared and thermal radiation shielding fabrics. Xu et al [19]. used silver-plated hollow glass microspheres doped with Al powder coating to prepare infrared stealth cotton fabric, which achieved excellent infrared stealth and thermal radiation protection properties. As a biomass fiber, bamboo fiber is more and more popular because of its high moisture absorption, excellent tensile strength and anti-ultraviolet properties [33]. However, the application of bamboo fiber in infrared stealth field has not been seen so far. In

addition, there are some problems such as high cost of organic solvent, difficulty in recovery and easy to cause environmental pollution for the process of electrospinning, which limits the development of textile industry [34, 35].

Herein, an antimony doped tin oxide/silver/bamboo fibers (ATO-Ag-BFs) composite fabrics with multi-functional properties such as infrared stealth, antibacterial and hydrophobic properties were prepared by the combination of ATO loading, chemical deposition and hot press process. The morphology, structure, and multi-functionality of ATO-Ag-BFs were investigated comprehensively by SEM, XPS, XRD and infrared emissivity testing. This work provides a new idea for the development of bio-based infrared stealth fabrics that are sustainable and environmentally friendly.

2. Materials and methods

2.1. Materials and reagents

Natural bamboo fibers (NBFs, about 1cm in average length) was acquired from Fujian Bamboo Fiber Material Technology Co., Ltd. (Fujian, China). Antimony doped tin oxide (ATO, average size: 20 nm, mass fraction of antimony: 10%)， potassium tartrate tetrahydrate, sodium citrate, ammonium hydroxide, silver nitrate, sodium hydroxide, and anhydrous ethanol were obtained from Guanghua Technology Co., Ltd. (Guangdong, China). γ-(2,3-epoxypropoxy) propytrimethoxysilane (KH560), n-hexadecyl mercaptan and sodium hexametaphosphate (SHMP) were acquired from Macklin Biochemical Co., Ltd. (Shanghai, China). Polyvinylpyrrolidone (PVP, M_w =1,300,000) was obtained from Aladdin Biochemical Co., Ltd. (Shanghai, China). All chemicals were used directly without purification. All experiments were performed using distilled

water made in the laboratory.

2.2. Pretreatment of NBFs

Before experiment, it is essential to treat the surface of NBFs with a certain concentration of alkali solution. The NBFs were soaked with 40.0 g L^{-1} sodium hydroxide at 65 °C for 30 min. This step was intended to achieve a rough and clean surface which was suitable for the further reaction. Afterwards, the alkali-treated NBFs were mechanically agitated to obtain fibers of small size and labeled as BFs.

2.3. Preparation of ATO-BFs

3.0 g SHMP and 10.0 g ATO nanoparticles were mixed in 500 mL deionized water and stirred at room temperature. During the stirring process, an anhydrous ethanol solution containing 20% KH560 was added slowly into the above solution until the mass ratio of KH560 and ATO was 1:10. The BFs were immersed in the solution for 30 min under ultrasonic oscillation at a power of 250 W and then under vacuum of –0.07 MPa for 20 min. After the reaction was completed, the BFs were rinsed to remove the unreacted ATO with distilled water. The ATO-loaded BFs were obtained and labeled as ATO-BFs after the filter cake was dried.

2.4. Preparation of ATO-Ag-BFs

The ATO-BFs and BFs were first immersed in 10.0 g L^{-1} $AgNO_3$ solution for 15 h and then reduced with 14.0 g L^{-1} PVP/anhydrous ethanol solution at 80 °C to acquire the silver seeds. Ammonium hydroxide was added to the above solution until the mixed solution was completely transparent, and at the same time 12.0 g L^{-1} sodium citrate solution as a complexing agent was added to acquire an electroless plating solution. The sensitized ATO-BFs and BFs were placed in

electroless plating solution, and 100.0 g L^{-1} potassium sodium tartrate solution was added tardily. After the completion of electroless plating, the ATO-BFs and BFs were washed with anhydrous ethanol and distilled water. The filter cakes were dried to acquire the electroless plating ATO-BFs and BFs, which were labeled as ATO-Ag-BFs and Ag-BFs.

2.5. Preparation of hot-pressed fabrics

The BFs, ATO-BFs, Ag-BFs, and ATO-Ag-BFs were hot-pressed at 5 MPa for 5 min to obtain the corresponding fabrics.

2.6. Hydrophobic treating

To prepare hydrophobic ATO-Ag-BFs fabrics, they were immersed in 50 mL of anhydrous ethanol solution containing 450 μL of n-cetyl mercaptan for 30 min. After drying at 80 °C for 24 h, the modified ATO-Ag-BFs were collected and labeled as H-ATO-Ag-BFs.

2.7. Bacteriostatic performance test

The antibacterial activities of BFs, ATO-BFs, Ag-BFs and ATO-Ag-BFs were evaluated by the quantities of colony-forming units (CFU). In detail, Luria−Bertani (LB) broth was acquired by adding beef extract (1.50 g) and trypsin (2.50 g) to 500 ml of deionized water. All samples were sterilized in an autoclave at 121°C for 25 min prior to the antimicrobial test. Then, 20 μL of *E. coli* and *S. aureus* bacterial strain were transferred to erlenmeyer flask containing 20 mL of LB broth, respectively. To provide sufficient activity, the above conical flasks incubated in a shaker of 150 rpm at 37 °C until the number of colonies reached 1×10^9, and then was diluted to 1×10^5 as a pre-inoculation solution. 0.15 g of samples were placed in a 50 mL flask containing 15 mL of 0.03 mol L^{-1} phosphate buffer solution and injected with 1×10^5 CFU mL^{-1} of bacteria, respectively.

The samples were incubated for 18 h at 37 °C with vigorous shaking. Finally, a count was carried out to confirm the number of bacteria living. The bacteriostatic rate (Y) was obtained according to Eq. (1)

$$Y(\%) = \frac{W_t - Q_t}{W_t} \times 100 \quad (1)$$

where W_t shows the value of the concentration of viable bacteria in the control samples. Q_t shows the value of concentration of viable bacteria in the test samples. When Y value is higher than 70%, the sample was considered to have considerable antibacterial effect [36].

2.8. Characterization of Materials

The crystallo-graphic structures and phase of BFs, ATO-BFs, Ag-BFs and ATO-Ag-BFs were collected by X-ray diffraction (XRD, Rigaku Ultima IV). Data were recorded from 2θ = 5–90° at a rate of 5° min^{-1}. The surface morphology of fabrics was characterized by SEM (TESCAN MIRA LMS, Czechia), and chemical mapping by EDS (Smartedx) to determine the composition of the fabric. The surface chemical/elemental state of the fibers was determined by X-ray photoelectron spectroscopy (XPS, Thermo Fisher Scientific K-Alpha). The infrared emissivity of the samples was collected with an infrared reflectance spectrometer (BURKE, USA). An optical contact angle measuring instrument (Theta Lite, iolin, Finland) was used to measure the water contact angle (WCA) of samples. Thermogravimetric analysis (TG, STA449F1, Netzsch) of fabrics were performed under nitrogen atmosphere. A universal material testing machine (Instron 3300, USA) were used to evaluate mechanical properties at room temperature. Thermal infrared camera (T-420, FLIR) was used to analyze the infrared and thermal radiation shielding properties by imaging fabrics.

3. Results and discussion

3.1. Morphology characterization of fibers

ATO-Ag-BFs composite fabrics were prepared by the combination of ATO loading, chemical deposition and hot press process as illustrated in Fig. 1, and the bonding mechanism of KH560 with ATO and BFs was proposed as shown in Fig. 2. This process involves the hydrolysis of the $-OCH_3$ group in KH560, which reacts with the −OH group on ATO to form a chemical bond, and the epoxide group ($-OCH_2CH$ (*O*) CH_2) in KH560 undergoes ring-opening polymerization with BFs [37]. The fibers prepared under four different conditions (BFs, ATO-BFs, Ag-BFs, ATO-Ag-BFs) were characterized by SEM and are presented in Fig. 3a–d. The BFs surface was relatively rough after alkali treatment, which provided a large quantity of active sites for ATO loading, ensuring the possibility of subsequent restructuring (Fig. 3a1 and a2). The ATO-BFs obtained by grafting reaction showed that ATO nanoparticles was randomly spread on the fibers surface in a spherical structure (Fig. 3b1 and b2). After electroless plating of silver, ATO and Ag nanoparticles were wrapped together on the fibers surface. Meanwhile, Ag nanoparticles were embedded in pores that were not encapsulated by ATO particles and formed a multi-layered structure on the fibers surface (Fig. 3d1, c1, d2 and c2).

The EDS element mapping and energy dispersive X-ray detector (EDX) spectrum were used to confirm the successful grafting of ATO and the loading of Ag. As shown in Fig. 3e–j, the distribution of C, N, O, Sn, Sb and Ag elements could be clearly observed, and Sn, Sb and Ag were uniformly deposited on the fibers. Notably, the mass ratio of C decreased from 60.13% to 41.86% of BFs after ATO grafting (Fig. 3k–l). The electroless silver plating further reduced the

mass ratio of C to 32.01% subsequently, while a similar phenomenon was observed for the mass ratio of O element. This was attributed to the introduction of inorganic substances, which reduced the relative content of O element.

3.2. Structure characterization of fibers

The composition of BFs, ATO-BFs, Ag-BFs and ATO-Ag-BFs was confirmed by XRD, as shown in Fig. 4a. The diffraction pattern of BFs at 2θ values of 16.0° and 22.3° were ascribed to (110) and (002) crystallographic plane of cellulose I, respectively [38-40]. The ATO-BFs, Ag-BFs and ATO-Ag-BFs showed similar diffraction patterns with BFs. Moreover, there are five additional diffraction peaks for ATO-BFs appeared at 26.7, 33.9, 38.1, 51.9 and 54.7°, belong to (110), (101), (200), (211), and (220) crystallographic planes of ATO (PDF card 71-0652) [41-43], respectively. The Ag-BFs had additional peaks at 2θ = 38.0, 44.3, 64.3, 77.3 and 81.6°, which correspond to (111), (200), (220), (311) and (222) diffraction peaks from silver (PDF card 87-6597) [19, 44]. However, in the XRD pattern of ATO-Ag-BFs, diffraction peaks of ATO and Ag can be seen at the same time, indicating that ATO and silver nanoparticles already exist in ATO-Ag-BFs, which was consistent with the results of EDS and SEM.

XPS analysis was further employed to determine the surface element state/chemical composition of the composite fibers. As shown in Fig. 4b, the characteristic peaks of Sn, Ag, O, and C peaks could be observed. Additionally, the XPS high-resolution curves of ATO-Ag-BFs were peak-fitted and shown in Fig. 4c–f. In the XPS spectra of C1s (Fig. 4c), three peaks at 284.8, 286.6 and 288.5 eV correspond to C–C/C–H species, C–O species and C=O/C−O−C species, respectively [28, 45]. Besides, the high-resolution XPS spectra of Sn and Sb (Fig. 4d–e) showed

the binding energies of Sn $3d_{5/2}$ and Sn $3d_{3/2}$ located at 486.6 eV and 495.0 eV, and those of Sb $3d_{5/2}$ and Sb $3d_{3/2}$ at 530.6 eV and 538.2 eV, respectively [46, 47]. Fig. 4f shows the XPS pattern of silver with two peaks at 368.2 and 373.9 eV, corresponding to Ag $3d_{5/2}$ and Ag $3d_{3/2}$, respectively [48]. Notably, the peak intensities of C1s and O1s of ATO-Ag-BFs were lower than BFs, which was attributed to the introduction of ATO and Ag as inorganic components. This was confirmed in the EDS analysis.

3.3. Infrared stealth performance of fabrics

The infrared emissivity is considered to be the main factor affecting the infrared stealth performance of fabrics. The lower the emissivity, the better the infrared stealth performance of the fabric. The infrared emissivity of all samples was tested at 3–5 μm, 8–14 μm and 14–22 μm. Among them, the emissivity value of ATO-Ag-BFs was the lowest in the three windows (Fig. 5a–c), with an average infrared emissivity of 0.68 in the 8–14 μm band. This emissivity allows a great integration of the target into the ambient background. The ATO-Ag-BFs exhibited lower infrared emissivity compared to ATO-BFs and Ag-BFs, which was attributed to the Schottky junctions formed by the contact between ATO and silver nanoparticles leading to the formation of (Fig. 6), which generated internal electric fields [17, 49, 50]. Therefore, photogenerated electrons and holes were produced at the contact interface and they moved in different directions to reduce the recombination rate of holes and electrons, which increased the carrier concentration. Due to the increase of carrier concentration on metal surface, the resonance wavelength of localized surface plasmon resonance (LSPR) was redshifted, and as a result, the infrared stealth performance of ATO-Ag-BFs was improved [51].

To verify the shielding effect of infrared and thermal radiation, a part of the human body was covered with a composite fabric, and infrared and thermal radiation emitted by the human body was captured with an infrared camera. Visible and infrared images of a person wearing a lab coat partially stitched with BFs, ATO-BFs, Ag-BFs and ATO-Ag-BFs fabrics are shown in Fig. 5d–e. The various infrared intensities that appeared on the lab coat are known from the infrared images, and these infrared intensities were determined by the human body temperature. Among BFs, ATO-BFs, Ag-BFs and ATO-Ag-BFs, the area where the ATO-Ag-BFs fabric was applied showed lower infrared intensity. It is noteworthy that the temperature in the dorsal region was ~29.8–32.5°C when measured with the infrared camera, while the temperature in the regions with ATO-BFs,Ag-BFs and ATO-Ag-BFs was ~28.5°C, ~27.1°C and ~26.7°C, respectively. The ambient temperature around the human body was ~25°C, which was similar to the temperature measured by applying the ATO-Ag-BFs fabric. Fig. 5f shows the infrared image of the four fabrics applied to the arm, which had the same effect as Fig. 5e. This confirmed that the ATO-BFs-based fabrics could effectively shield the infrared and thermal radiation produced by the human body. In addition, the visible and infrared images of the index finger wrapped with ATO-Ag-BFs fabric are shown in Fig. 5g–h. Compared to the infrared emitted by the hand, the part wrapped with the ATO-Ag-BFs fabric looks as if part of the finger has been severed. The temperature of the finger dropped from 32.6 to 26.7 °C, with a decrease of ~6°C. However, the effects of harsh environments need to be considered in practical applications, so the durability of infrared shielding was explored in the test range of 20–80 °C and was shown in Fig. 5i. Among all fabrics, ATO-Ag-BFs had the lowest temperature change interval from 18.8 to 55.7 °C, with a change of 36.9 °C, which was only half

of the applied temperature. These results confirmed that ATO-Ag-BFs fabrics exhibit considerable performance in terms of infrared and thermal radiation shielding.

3.4. Antibacterial Performance of fabrics

The national standard (GB/T 20944.3-2008) for antimicrobial properties of textiles was used to evaluate the antimicrobial activity under different modified conditions. The results of antimicrobial tests are shown in Fig. 7a–b and Table 1. In the blank control group, the colony counts of *E. coli* and *S. aureus* reached 4.22×10^7 and 3.82×10^5, respectively, after 18 h of cultivation. Compared with the blank sample, no significant change was found in the number of colonies in BFs, so BFs did not have effective antibacterial properties. After ATO grafting, the number of colonies of *E. coli* and *S. aureus* reduced to 5.65×10^6 and 4.0×10^4, respectively. This antibacterial effect might be attributed to the fact that the dissolution of Sn^{4+} ions could disrupt cell activities and tissues [52]. Therefore, the inhibition rates of ATO-BFs against *E. coli and S. aureus* were 86.15% and 78.38%, respectively (Fig. 7c–d). However, the antibacterial effect of ATO-Ag-BFs was significantly enhanced by the introduction of silver nanoparticles after the modification by chemical silver plating. It exhibited a 100% inhibition rate against *E. coli* and *S. aureus*, which has already outperformed most of the antimicrobial available textile materials [53]. The reasons for the marked enhancement in antimicrobial performances was the presence of the Schottky junction that promote the separation of holes and photogenerated electrons on the ATO surface. The synergistic antibacterial effect was achieved precisely by the reaction of these free electrons with O_2 to form $\bullet O^{2-}$ while reacted with H_2O to form $\bullet OH$, which directly damages the

cell membrane of bacteria [54]. In general, ATO-BFs has excellent antibacterial effect, which provides a feasible approach for further biomedical applications.

3.5. Hydrophobic performance of fabrics

The hydrophobicity is essential for fibers to maintain a degree of shielding from infrared and thermal radiation. Water absorption would cause distortion of the infrared image when the fibers are exposed to water. The WCA test was used to test the hydrophobic property of samples. As shown in Fig. 8a, the unmodified BFs showed considerable hydrophilicity, and its surface could be directly wetted by liquids. The WCA of ATO-BFs and Ag-BFs increased to 15.6° and 23.3° after ATO grafting or chemical silver plating, respectively, which was attributed to the coverage of ATO or Ag nanoparticles on the fibers surface. Moreover, when ATO and Ag were introduced into BFs simultaneously, the contact angle of ATO-Ag-BFs increased to 39.5°. It revealed that the WCA value improved with the increase of roughness. The surface roughness would expand the wettability of the original surface, which was in accordance with the Wenzel model [55]. However, it was promising that the hydrophobically treated H-ATO-Ag-BFs exhibited excellent hydrophobic property with a WCA of 147.7° (Fig. 8b) in all areas. As a result, the droplets on the surface of the fabric were not penetrated, but tended to slip off.

3.6. Mechanical and thermal performance analysis of fabrics

The typical stress–strain curves and corresponding tensile strength, Young's modulus for BFs, ATO-BFs, Ag-BFs and ATO-Ag-BFs are described in Fig. 9a–b. Compared with other fabrics, BFs have the highest mechanical strength as can be seen in Fig. 9a. And corresponding tensile strength and Young's modulus was 5.1 MPa and 252.3 MPa (Fig. 9b). After incorporation of ATO and Ag,

due to the disruption of hydrogen bonds between the fibers, the tensile strength and Young's modulus of ATO-Ag-BFs reduced to 3 MPa and 131 MPa, respectively [10].

Fig. 9c–d show the TGA-DTG curves of BFs, ATO-BFs, Ag-BFs and ATO-Ag-BFs. The initial weight loss before 100 °C was caused by the evaporation of water in bamboo fibers. The range from 100 to 380 °C was the main mass loss region for cellulose, hemicellulose and lignin in bamboo. The range from 380 to 600 °C was the carbonization zone, which was the process of further degradation of $_{L}$-glucose, leading to the production of low molecular weight products [56]. When the temperature rised to 800 °C, the high melting point ATO was degraded after the degradation of bamboo fibers, which resulted in further mass loss of ATO-BFs and ATO-Ag-BFs [15]. When the temperature was higher than 800 °C, only high melting point Ag was remained and no further weight loss occurred [19]. Thus, when the reference temperature was 1000 °C, the final remaining mass in the TGA and DTG analysis plots were 7.6% (BFs), 28.5% (ATO-Ag-BFs), 22.6% (Ag-BFs) and 37.8% (ATO-Ag-BFs), respectively.

4. Conclusion

In this study, an antimony doped tin oxide/silver/bamboo fibers (ATO-Ag-BFs) composite fabrics with multi-functional properties such as infrared stealth, antibacterial and hydrophobic properties were prepared by the combination of ATO loading, chemical deposition and hot press process. The contact of ATO nanoparticles with Ag nanoparticles formed Schottky junctions on the fiber surface, which improved the carrier concentration and formed the absorption of infrared light by LSPR. The infrared emissivity was as low as 0.68 in the 8–14 μm thermal imaging band.

When ATO-Ag-BFs were applied to the human index finger, the surface temperature of the fabric was reduced by ~6°C compared to the infrared intensity emitted by the human body. For another, ATO and Ag nanoparticles exhibited synergistic antibacterial effects, resulting in 100% inhibition rate of ATO-Ag-BFs against *E. coli* and *S. aureus*. Besides, the maximum WCA of hydrophobically treated ATO-Ag-BFs was 147.7°, resulting in a tendency for droplets on the fabric surface to slip off. To sum up, composite fibers based on environmentally friendly bamboo fibers (ATO-Ag-BFs) are expected to lead a new direction for wearable infrared stealth products with versatility.

Authors' contributions

Xin-Yao Ye: Conceptualization, Formal analysis, Writing – original draft. Yu Chen: Conceptualization, Methodology. Jing Yang: Conceptualization, Methodology. Hai-Yan Yang: Writing—review and editing, Methodology. Da-Wei Wang: Methodology, Validation. Ben Bin Xu: paper revision and technique check. Junna Ren: Sample checking and data analysis. Deepak Sridhar: data analysis, reveiw and fromat. Zhanhu Guo: Conceptualization, Review and editing. Zheng-Jun Shi: Conceptualization, Funding acquisition, Methodology, Project administration.

Funding

This work was supported by the National Natural Science Foundation of China (No. 31971741, 31760195), the Yunnan Fundamental Research Projects (No. 202001AT070141), and Yunnan Agricultural Basic Research Special Projects (grant No. 202101BD070001-086).

Declarations

Conflict of interest The authors declare no competing interests.

References

1. Zhou Y-C, Yang J, Bai L et al (2022) Flexible phase change hydrogels for mid-/low-temperature infrared stealth. Chem Eng J 446: 137463. https://doi.org/10.1016/j.cej.2022.137463

2. Lyu J, Liu Z, Wu X et al (2019) Nanofibrous kevlar aerogel films and their phase-change composites for highly efficient infrared stealth. ACS Nano 13(2): 2236–2245. https://doi.org/10.1021/acsnano.8b08913

3. Cui Y, Gong H, Wang Y et al (2018) A thermally insulating textile inspired by polar bear hair. Adv Mater 30(14): 1706807. https://doi.org/10.1002/adma.201706807

4. Wen XY, Liu Z, Wang J et al (2019) Nanocomposite hydrogels with optic-sonic transparency and hydroacoustic-sensitive conductivity for potential antiscouting sonar. ACS Appl Mater Interfaces 11(22): 20386–20393. https://doi.org/10.1021/acsami.9b04463

5. Balci O, Polat EO, Kakenov N et al (2015) Graphene-enabled electrically switchable radar-absorbing surfaces. Nat Commun 6(1): 6628. https://doi.org/10.1038/ncomms7628

6. Hu J, Hu Y, Ye Y et al (2023) Unique applications of carbon materials in infrared stealth: A review. Chem Eng J 452(Part 1): 139147. https://doi.org/10.1016/j.cej.2022.139147

7. Wu Y, Zhao Y, Zhou M et al (2022) Ultrabroad microwave absorption ability and infrared stealth property of nano-micro CuS@rGO lightweight aerogels. Nano-Micro Lett 14(1): 171. https://doi.org/10.1007/s40820-022-00906-5

8. Park C, Kim J, Hahn JW (2020) Selective emitter with engineered anisotropic radiation to minimize dual-band thermal signature for infrared stealth technology. ACS Appl Mater

Interfaces 12(38): 43090–43097. https://doi.org/10.1021/acsami.0c12283

9. Liu Y, Zuo H, Xi W et al (2021) Flexible janus functional film for adaptive thermal camouflage. Adv Mater Technol 7(3): 2100821. https://doi.org/10.1002/admt.202100821

10. Jeong S-M, Ahn J, Choi YK et al (2020) Development of a wearable infrared shield based on a polyurethane–antimony tin oxide composite fiber. NPG Asia Mater 12: 32. https://doi.org/10.1038/s41427-020-0213-z

11. Karim S, Tong G, Li J et al (2023) Current advances and future perspectives of image fusion: A comprehensive review. Inform Fusion 90: 185–217. https://doi.org/10.1016/j.inffus.2022.09.019

12. Zhu H, Li Q, Zheng C et al (2020) High-temperature infrared camouflage with efficient thermal management. Light Sci Appl 9: 60. https://doi.org/10.1038/s41377-020-0300-5

13. Salihoglu O, Uzlu HB, Yakar O et al (2018) Graphene-based adaptive thermal camouflage. Nano Lett 18(7): 4541–4548. https://doi.org/10.1021/acs.nanolett.8b01746

14. Qu Y, Li Q, Cai L et al (2018) Thermal camouflage based on the phase-changing material GST. Light Sci Appl 7: 26. https://doi.org/10.1038/s41377-018-0038-5

15. Ahn J, Lim T, Yeo CS et al (2019) Infrared invisibility cloak based on polyurethane-tin oxide composite microtubes. ACS Appl Mater Interfaces 11(15): 14296–14304. https://doi.org/10.1021/acsami.8b22535

16. Wu J, Hu R, Zeng S et al (2020) Flexible and robust biomaterial microstructured colored textiles for personal thermoregulation. ACS Appl Mater Interfaces 12(16): 19015–19022. https://doi.org/10.1021/acsami.0c02300

17. Wang H, Ma Y, Qiu J et al (2021) Multifunctional PAN/Al–ZnO/Ag nanofibers for infrared stealth, self-cleaning, and antibacterial applications. ACS Appl Nano Mater 5(1): 782–790. https://doi.org/10.1021/acsanm.1c03518

18. Miao D, Jiang S, Shang S et al (2014) Effect of heat treatment on infrared reflection property of Al-doped ZnO films. Sol Energy Mater Sol Cells 127: 163–168. https://doi.org/10.1016/j.solmat.2014.04.030

19. Xu R, Wang W, Yu D (2019) Preparation of silver-plated hollow glass microspheres and its application in infrared stealth coating fabrics. Prog Org Coat 131: 1–10. https://doi.org/10.1016/j.porgcoat.2019.02.009

20. Wang Y, Li X, Wang C et al (2022) Preparation and characteristics of polymer matrix composite coatings with low infrared emissivity and high-temperature resistance. Polym Eng Sci 62(6): 1941–1949. https://doi.org/10.1002/pen.25977

21. Gu J, Wang W, Yu D (2021) Temperature control and low infrared emissivity double-shell phase change microcapsules and their application in infrared stealth fabric. Prog Org Coat 159: 106439. https://doi.org/10.1016/j.porgcoat.2021.106439

22. Shi HG, Zhao HB, Liu BW et al (2021) Multifunctional flame-retardant melamine-based hybrid foam for infrared stealth, thermal insulation, and electromagnetic interference shielding. ACS Appl Mater Interfaces 13(22): 26505–26514. https://doi.org/10.1021/acsami.1c07363

23. Mao Z, Wang W, Liu Y et al (2014) Infrared stealth property based on semiconductor (M)-to-metallic (R) phase transition characteristics of W-doped VO_2 thin films coated on cotton

fabrics. Thin Solid Films 558: 208–214. https://doi.org/10.1016/j.tsf.2014.02.055

24. Zhang Y, Qin Y, Quan B et al (2021) Simultaneous low reflection in near-infrared range and low emission in long-wave infrared properties of Al/Bi_2O_3 composites. Ceram Int 47(22): 31180–31186. https://doi.org/10.1016/j.ceramint.2021.07.293
25. Fan Q, Zhang L, Xing H et al (2020) Microwave absorption and infrared stealth performance of reduced graphene oxide-wrapped Al flake. J Mater Sci Mater Electron 31(4): 3005–3016. https://doi.org/10.1007/s10854-019-02844-2
26. Jiang S, Miao D, Xu J et al (2016) Preparation and characterization of shielding textiles to prevent infrared penetration with Ag thin films. J Mater Sci Mater Electron 28(4): 3542–3547. https://doi.org/10.1007/s10854-016-5955-6
27. Tan P, Li H, Wang J et al (2021) Silver nanoparticle in biosensor and bioimaging: Clinical perspectives. Biotechnol Appl Bioc 68(6): 1236–1242. https://doi.org/10.1002/bab.2045
28. Hong G, Cheng H, Zhang K et al (2022) Cleaner production strategy tailored versatile biocomposites for antibacterial application and electromagnetic interference shielding. J Clean Prod 366: 132835. https://doi.org/10.1016/j.jclepro.2022.132835
29. Yuan L, Weng X, Deng L (2013) Influence of binder viscosity on the control of infrared emissivity in low emissivity coating. Infrared Phys Technol 56: 25–29. https://doi.org/10.1016/j.infrared.2012.09.004
30. Mao Z, Yu X, Zhang L et al (2014) Novel infrared stealth property of cotton fabrics coated with nano ZnO: (Al, La) particles. Vacuum 104: 111–115. https://doi.org/10.1016/j.vacuum.2014.01.011

31. Qiu Z, Xiao Z, Gao L et al (2019) Transparent wood bearing a shielding effect to infrared heat and ultraviolet via incorporation of modified antimony-doped tin oxide nanoparticles. Compos Sci Technol 172: 43–48. https://doi.org/10.1016/j.compscitech.2019.01.005

32. Qi Y, Yin X, Zhang J (2016) Transparent and heat-insulation plasticized polyvinyl chloride (PVC) thin film with solar spectrally selective property. Sol Energy Mater Sol Cells 151: 30–35. https://doi.org/10.1016/j.solmat.2016.02.016

33. Castanet E, Li Q, Dumée LF et al (2016) Structure–property relationships of elementary bamboo fibers. Cellulose 23(6): 3521–3534. https://doi.org/10.1007/s10570-016-1078-8

34. Avossa J, Herwig G, Toncelli C et al (2022) Electrospinning based on benign solvents: current definitions, implications and strategies. Green Chem 24(6): 2347–2375. https://doi.org/10.1039/d1gc04252a

35. Li Y, Liao C, Tjong SC (2019) Electrospun polyvinylidene fluoride-based fibrous scaffolds with piezoelectric characteristics for bone and neural tissue engineering. Nanomaterials 9(7): 952. https://doi.org/10.3390/nano9070952

36. Ye X-Y, Zhu E-Q, Wang D-W et al (2022) Cationic functionalized bamboo fibers with spinnable and antibacterial properties prepared in chlorocholine chloride/urea deep eutectic solvent. Ind Crops Prod 188: 115607. https://doi.org/10.1016/j.indcrop.2022.115607

37. Zhang M, Lyu J, Zuo Y et al (2023) Effect of KH560 concentration on adhesion between silicate modified poplar and waterborne varnish. Prog Org Coat 174: 107267. https://doi.org/10.1016/j.porgcoat.2022.107267

38. Hong G, Cheng H, Zhang S et al (2021) Mussel-inspired reinforcement of a biodegradable

aliphatic polyester with bamboo fibers. J Clean Prod 296: 126587. https://doi.org/10.1016/j.jclepro.2021.126587

39. Fang X, Li Y, Zhao J et al (2022) Improved interfacial performance of bamboo fibers/polylactic acid composites enabled by a self-supplied bio-coupling agent strategy. J Clean Prod 380(Part 1): 134719. https://doi.org/10.1016/j.jclepro.2022.134719

40. Kwak HW, Lee H, Lee ME et al (2018) Facile and green fabrication of silk sericin films reinforced with bamboo-derived cellulose nanofibrils. J Clean Prod 200: 1034–1042. https://doi.org/10.1016/j.jclepro.2018.07.289

41. Du Y, Zhang Y, Li L et al (2021) Nano SnO_2 and Sb_2O_3 combined with CNTs as a high-capacity lithium storage material. Appl Surf Sci 543: 148870. https://doi.org/10.1016/j.apsusc.2020.148870

42. Lv Y, Yang C, Wang H et al (2020) Antimony-doped tin oxide as an efficient electrocatalyst toward the VO^{2+}/VO^{+} redox couple of the vanadium redox flow battery. Catal Sci Technol 10(8): 2484–2490. https://doi.org/10.1039/c9cy01793c

43. Kim J, Murdoch BJ, Partridge JG et al (2020) Ultrasonic spray pyrolysis of antimony-doped tin oxide transparent conductive coatings. Adv Mater Interfaces 7(18): 2000655. https://doi.org/10.1002/admi.202000655

44. Ohta S, Mitsuhashi K, Chandel AKS et al (2022) Silver-loaded carboxymethyl cellulose nonwoven sheet with controlled counterions for infected wound healing. Carbohydr Polym 286: 119289. https://doi.org/10.1016/j.carbpol.2022.119289

45. Tong C, Zhang S, Zhong T et al (2021) Highly fibrillated and intrinsically flame-retardant

nanofibrillated cellulose for transparent mineral filler-free fire-protective coatings. Chem Eng J 419: 129440. https://doi.org/10.1016/j.cej.2021.129440

46. Bai H, Guo H, Wang J et al (2021) Hydrogen gas sensor based on SnO_2 nanospheres modified with Sb_2O_3 prepared by one-step solvothermal route. Sens Actuators B Chem 331: 129441. https://doi.org/10.1016/j.snb.2021.129441

47. Cao S, Guan Z, Feng Y et al (2022) S-doped Sb_2O_3 nanorods for electrocatalytic nitrogen reduction. ACS Appl Nano Mater 5(3): 3591–3598. https://doi.org/10.1021/acsanm.1c04177

48. Tan Y, Sun L, Wang G et al (2022) A two-step nonthermal plasma method to fabricate Ag/N-doped TiO_2/CNTs for formaldehyde removal under visible light irradiation. J Clean Prod 370: 133507. https://doi.org/10.1016/j.jclepro.2022.133507

49. Shahidi MM, Rezagholipour Dizaji H, Ehsani MH et al (2020) Effect of GLAD technique on optical and electrical properties of SnO_2/Ag/SnO_2 structure. Infrared Phys Technol 106: 103263. https://doi.org/10.1016/j.infrared.2020.103263

50. Cao W, Ma W, Lu T et al (2022) Multifunctional nanofibrous membranes with sunlight-driven self-cleaning performance for complex oily wastewater remediation. J Colloid Interface Sci 608(1): 164–174. https://doi.org/10.1016/j.jcis.2021.09.194

51. Bukasov R, Shumaker-Parry JS (2009) Silver nanocrescents with infrared plasmonic properties as tunable substrates for surface enhanced infrared absorption spectroscopy. Anal Chem 81(11): 4531–4535.

52. Haq S, Ahmad P, Khandaker MU et al (2021) Antibacterial, antioxidant and physicochemical investigations of tin dioxide nanoparticles synthesized via microemulsion method. Mater Res

Express 8(3): 035013. https://doi.org/10.1088/2053-1591/abed8a

53. Lem KW, Choudhury A, Lakhani AA et al (2012) Use of nanosilver in consumer products. Recent Pat Nanotechnol 6(1): 60–72.

54. Karki HP, Ojha DP, Joshi MK et al (2018) Effective reduction of p-nitrophenol by silver nanoparticle loaded on magnetic Fe_3O_4/ATO nano-composite. Appl Surf Sci 435: 599–608. https://doi.org/10.1016/j.apsusc.2017.11.166

55. Peng S, Bhushan B (2016) Mechanically durable superoleophobic aluminum surfaces with microstep and nanoreticula hierarchical structure for self-cleaning and anti-smudge properties. J Colloid Interface Sci 461: 273–284. https://doi.org/10.1016/j.jcis.2015.09.027

56. Lin Q, Huang Y, Yu W (2021) Effects of extraction methods on morphology, structure and properties of bamboo cellulose. Ind Crops Prod 169: 113640. https://doi.org/10.1016/j.indcrop.2021.113640

Table Captions

Table 1

Antibacterial test results

Sample	Bacterium	Dilution ratio	N after 18 h incubation (CPU mL^{-1})	Antibacterial Rate (%)
Black control	*E. coli*	1×10^4	4.22×10^7	/
BFs	*E. coli*	1×10^4	4.08×10^7	/
ATO-BFs	*E. coli*	1×10^4	5.65×10^6	86.15
Ag-BFs	*E. coli*	1×10^4	0	100
ATO-Ag-BFs	*E. coli*	1×10^4	0	100
Black control	*S. aureus*	1×10^3	3.82×10^5	/
BFs	*S. aureus*	1×10^3	1.85×10^5	/
ATO-BFs	*S. aureus*	1×10^3	4.0×10^4	78.38
Ag-BFs	*S. aureus*	1×10^3	0	100
ATO-Ag-BFs	*S. aureus*	1×10^3	0	100

Figure Legends

Fig. 1. Diagram of ATO-BFs, Ag-BFs and ATO-Ag-BFs preparation.

Fig. 2. Proposed bonding mechanism of KH560 with ATO and BFs.

Fig. 3. SEM images of BFs, ATO-BFs, Ag-BFs, and ATO-Ag-BFs at low (a1, b1, c1 and d1) and high (a2, b2, c2 and d2) resolution; (e) EDS analysis of ATO-Ag-BFs (C); (f) EDS analysis of ATO-Ag-BFs (N); (g) EDS analysis of ATO-Ag-BFs (O); (h) EDS analysis of ATO-Ag-BFs (Sn); (i) EDS analysis of ATO-Ag-BFs (Sb); (j) EDS analysis of ATO-Ag-BFs (Ag); (k) Elemental mass ratio of BFs, ATO-BFs, Ag-BFs and ATO-Ag-BFs; and (l) DES energy spectra of ATO-Ag-BFs.

Fig. 4. (a) XRD spectra of BFs, ATO-BFs, Ag-BFs and ATO-Ag-BFs; (b) XPS wide-scan spectra of BFs, ATO-BFs, Ag-BFs and ATO-Ag-BFs; (c) C1s core-level of ATO-Ag-BFs; (d) Sn 3d core-level of ATO-Ag-BFs; (e) Sb 3d core-level of ATO-Ag-BFs; and (f) Ag 3d core-level of ATO-Ag-BFs.

Fig. 5. Infrared emissivity of BFs, ATO-BFs, Ag-BFs and ATO-Ag-BFs at three windows of (a) 5−8 μm; (b) 8−14 μm; (c) 14−24 μm; (d) Visible-light images of fabrics based on BFs, ATO-BFs, Ag-BFs and ATO-Ag-BFs applied to the lab coat; (e) and (f) Infrared images of BFs, ATO-BFs, Ag-BFs and ATO-Ag-BFs; (g) and (h) are the visible and infrared images of a finger partially wrapped with ATO-Ag-BFs, respectively; and (i) The temperatures of BFs, ATO-BFs, Ag-BFs and ATO-Ag-BFs were measured at application temperatures ranging from 20 to 80°C.

Fig. 6. The formation process of Schottky junction between SnO_2 and Ag.

Fig. 7. The antibacterial activities photography of BFs, ATO-BFs and ATO-Ag-BFs against bacteria (a) *E. coli*; and (b) *S. aureus*; (c) and (d) The inhibition rate of these samples against *E. coli* and *S. aureus*.

Fig. 8. (a) Water contact angle of BFs, ATO-BFs, Ag-BFs, ATO-Ag-BFs and H- ATO-Ag-BFs; and (b) Visible image of the water contact angle of H-ATO-Ag-BFs.

Fig. 9. (a) and (b) Stress-strain curves, tensile strength, and Young's modulus for BFs, ATO-BFs, Ag-BFs, and ATO-Ag-BFs, respectively; (c) and (d) TGA and DTG curves of BFs, ATO-BFs, Ag-BFs, and ATO-Ag-BFs.

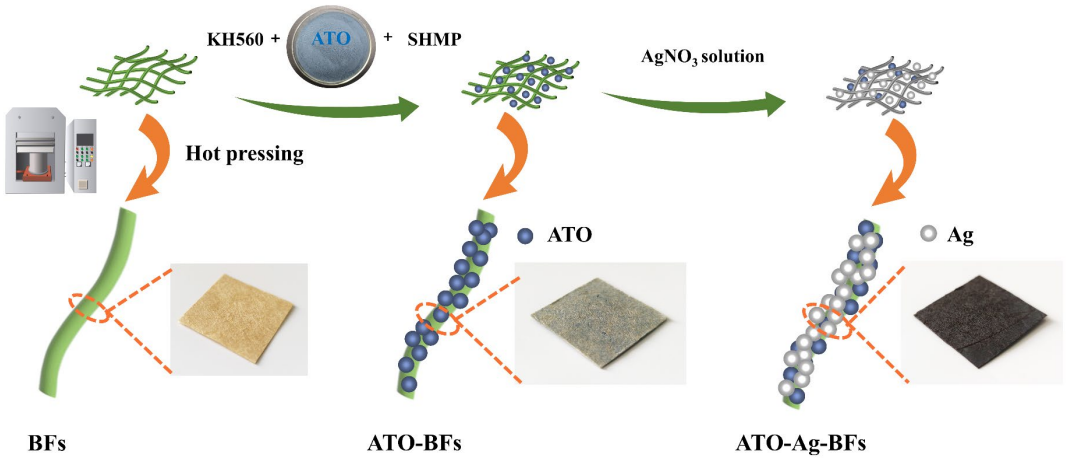

Fig. 1. Diagram of ATO-BFs, Ag-BFs and ATO-Ag-BFs preparation.

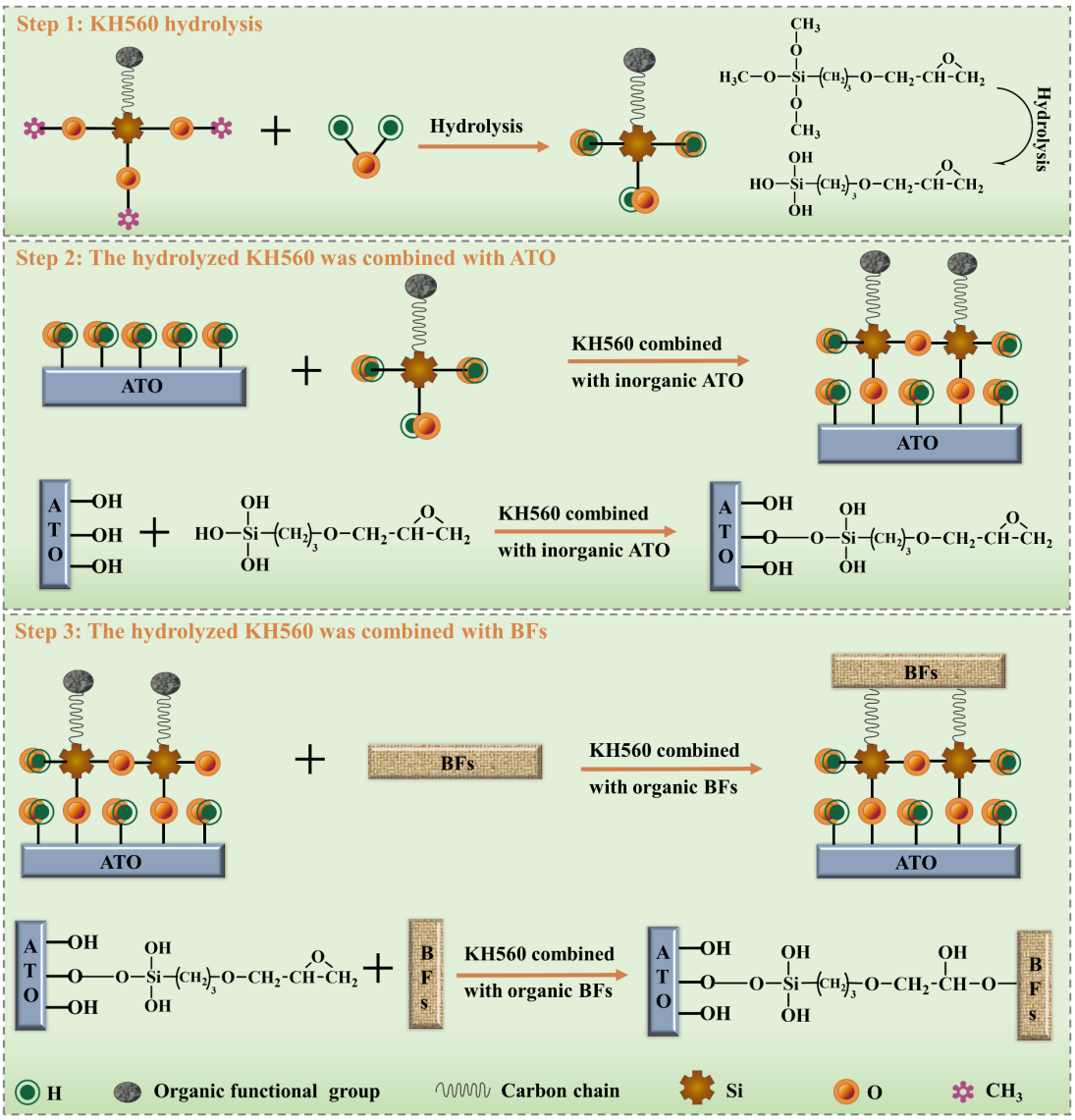

Fig. 2. Proposed bonding mechanism of KH560 with ATO and BFs.

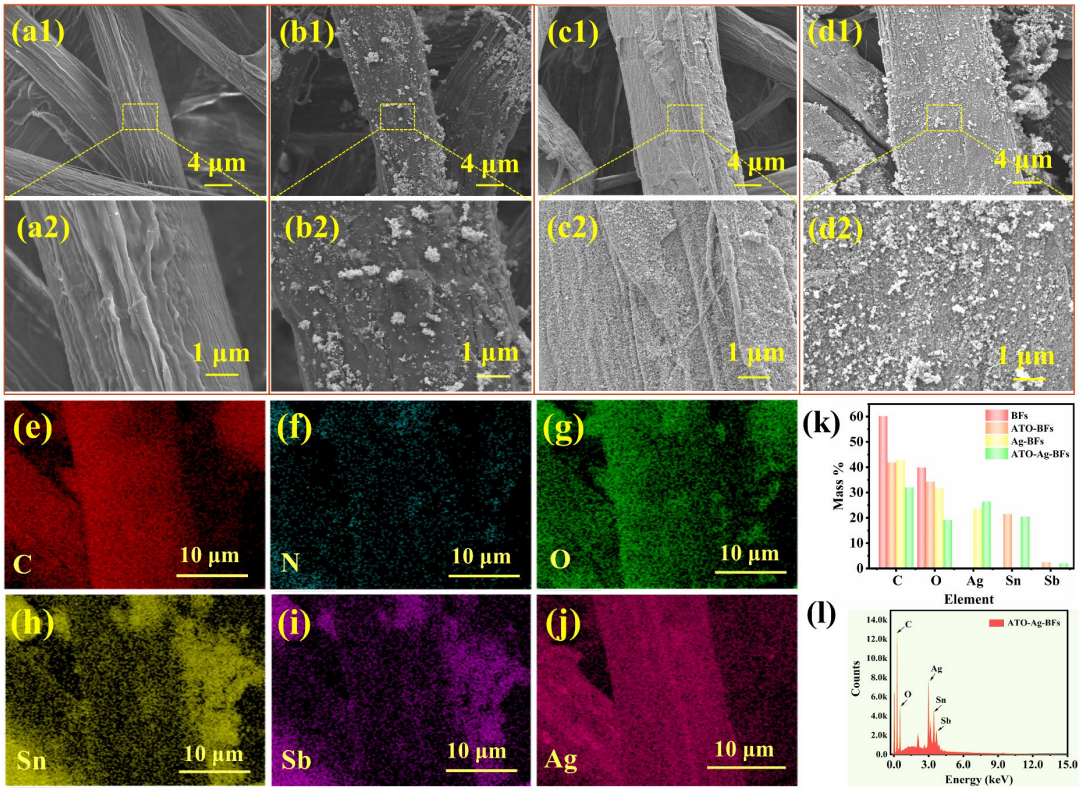

Fig. 3. SEM images of BFs, ATO-BFs, Ag-BFs, and ATO-Ag-BFs at low (a1, b1, c1 and d1) and high (a2, b2, c2 and d2) resolution; (e) EDS analysis of ATO-Ag-BFs (C); (f) EDS analysis of ATO-Ag-BFs (N); (g) EDS analysis of ATO-Ag-BFs (O); (h) EDS analysis of ATO-Ag-BFs (Sn); (i) EDS analysis of ATO-Ag-BFs (Sb); (j) EDS analysis of ATO-Ag-BFs (Ag); (k) Elemental mass ratio of BFs, ATO-BFs, Ag-BFs and ATO-Ag-BFs; and (l) DES energy spectra of ATO-Ag-BFs.

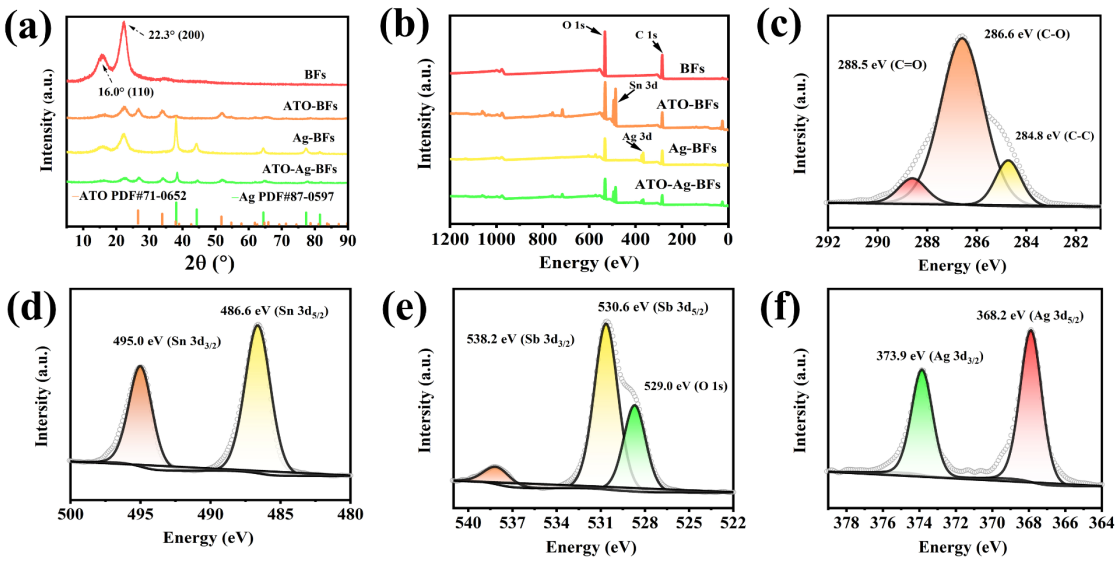

Fig. 4. (a) XRD spectra of BFs, ATO-BFs, Ag-BFs and ATO-Ag-BFs; (b) XPS wide-scan spectra of BFs, ATO-BFs, Ag-BFs and ATO-Ag-BFs; (c) C1s core-level of ATO-Ag-BFs; (d) Sn 3d core-level of ATO-Ag-BFs; (e) Sb 3d core-level of ATO-Ag-BFs; and (f) Ag 3d core-level of ATO-Ag-BFs.

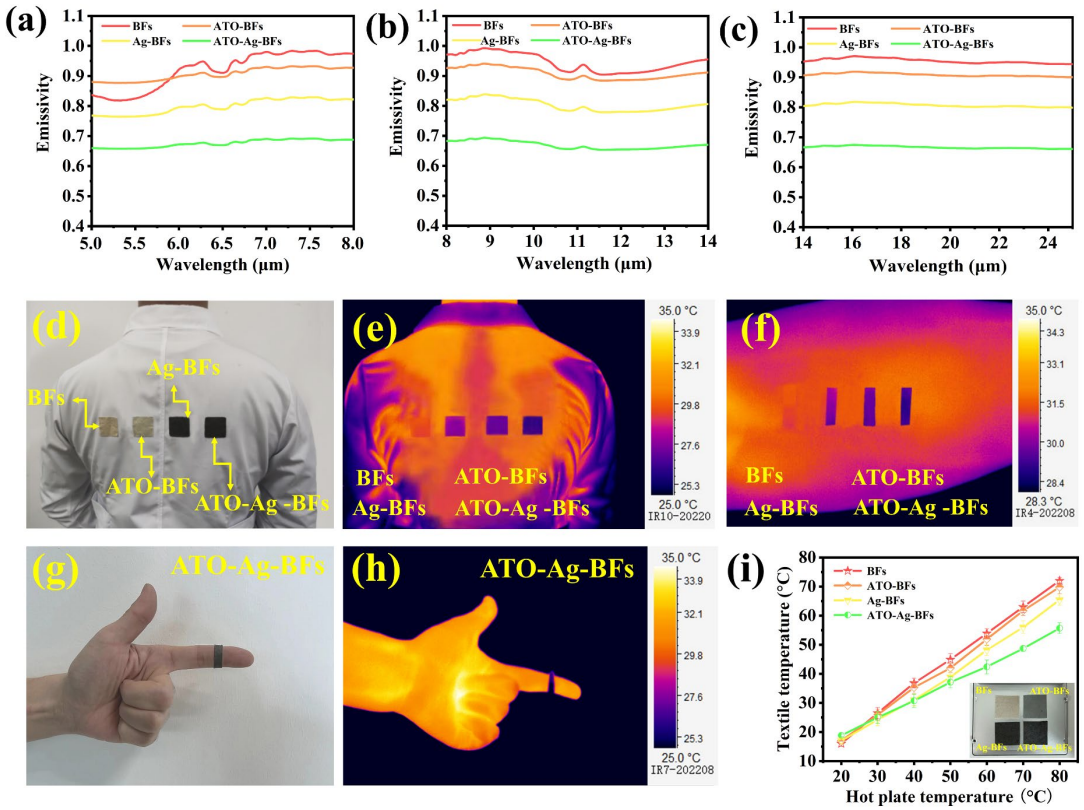

Fig. 5. Infrared emissivity of BFs, ATO-BFs, Ag-BFs and ATO-Ag-BFs at three windows of (a) 5−8 μm; (b) 8−14 μm; (c) 14−24 μm; (d) Visible-light images of fabrics based on BFs, ATO-BFs, Ag-BFs and ATO-Ag-BFs applied to the lab coat; (e) and (f) Infrared images of BFs, ATO-BFs, Ag-BFs and ATO-Ag-BFs; (g) and (h) are the visible and infrared images of a finger partially wrapped with ATO-Ag-BFs, respectively; and (i) The temperatures of BFs, ATO-BFs, Ag-BFs and ATO-Ag-BFs were measured at application temperatures ranging from 20 to 80 °C.

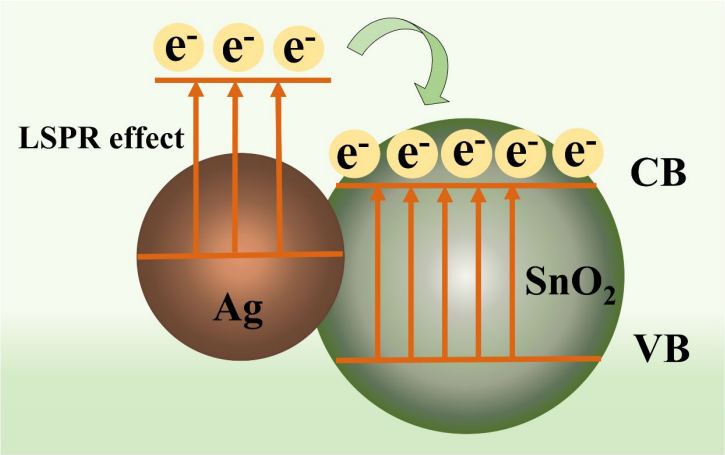

Fig. 6. The formation process of Schottky junction between SnO_2 and Ag.

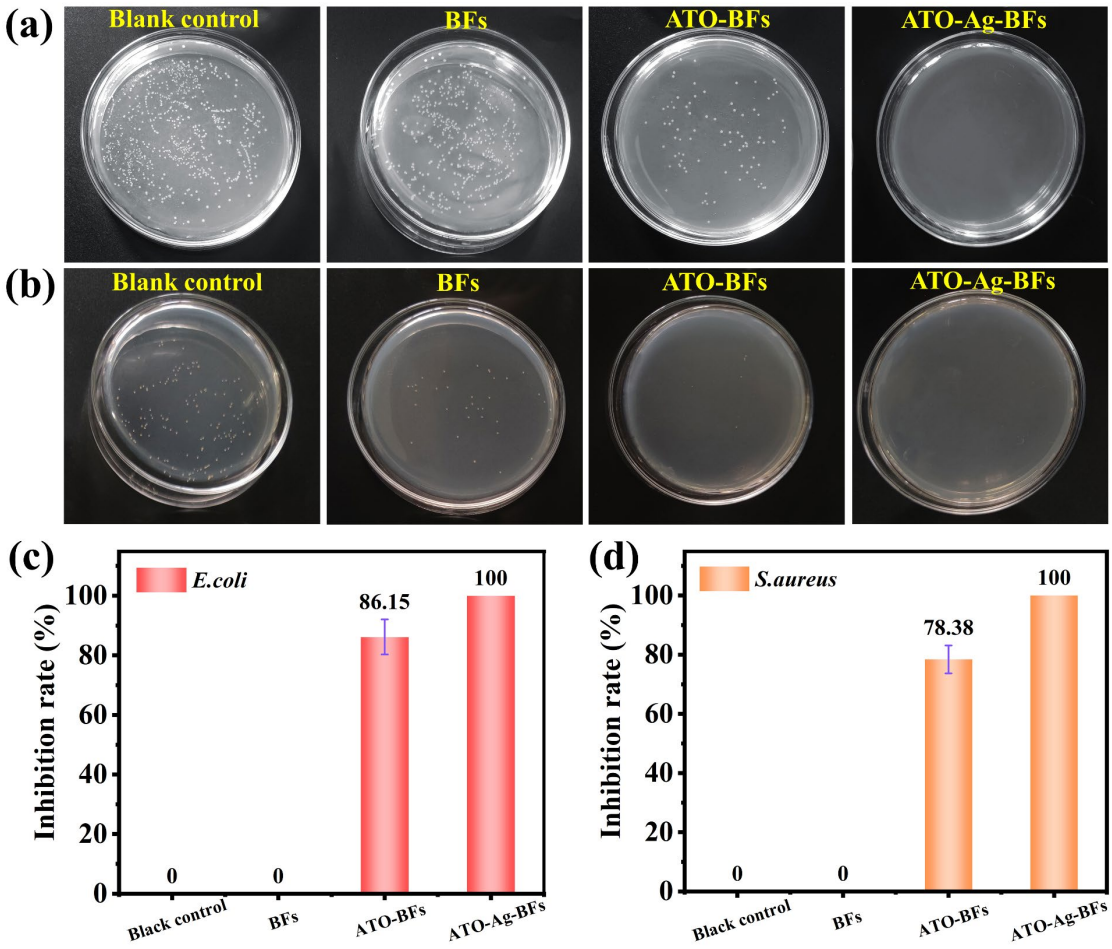

Fig. 7. The antibacterial activities photography of BFs, ATO-BFs and ATO-Ag-BFs against bacteria (a) *E. coli*; and (b) *S. aureus*; (c) and (d) The inhibition rate of these samples against *E. coli* and *S. aureus*.

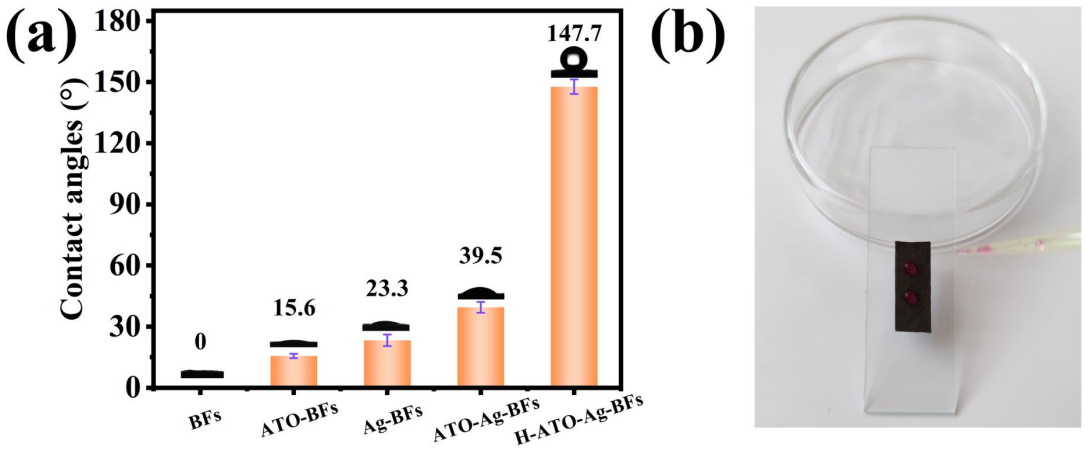

Fig. 8. (a) Water contact angle of BFs, ATO-BFs, Ag-BFs, ATO-Ag-BFs and H- ATO-Ag-BFs; and (b) Visible image of the water contact angle of H-ATO-Ag-BFs.

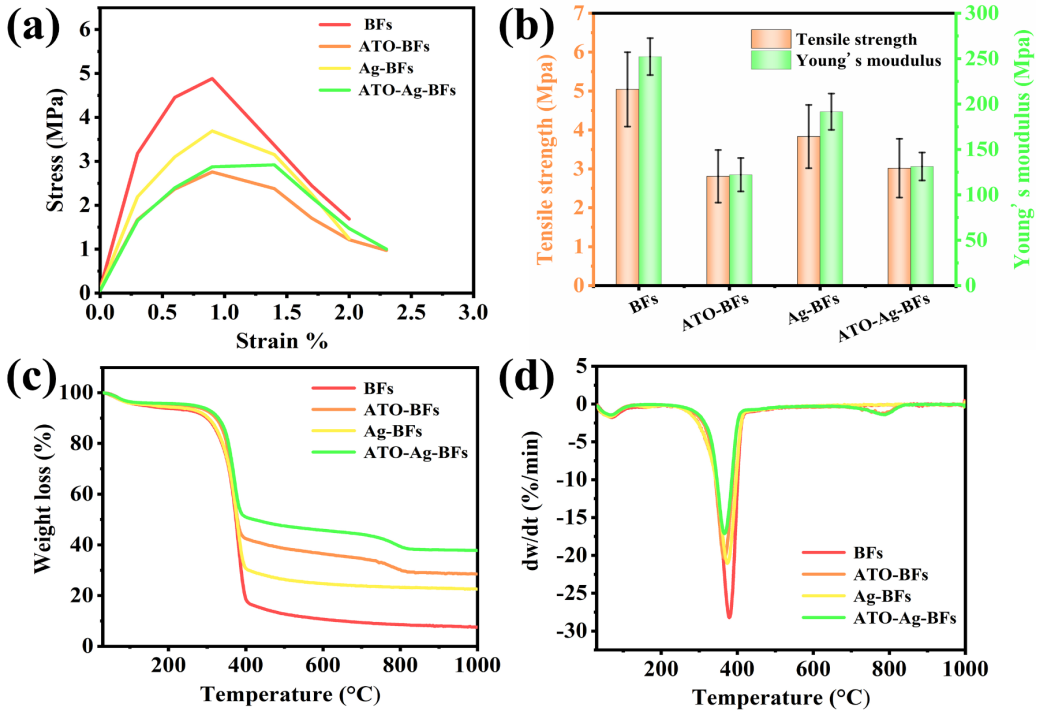

Fig. 9. (a) and (b) Stress-strain curves, tensile strength, and Young's modulus for BFs, ATO-BFs, Ag-BFs, and ATO-Ag-BFs, respectively; (c) and (d) TGA and DTG curves of BFs, ATO-BFs, Ag-BFs, and ATO-Ag-BFs.

Graphical Abstract

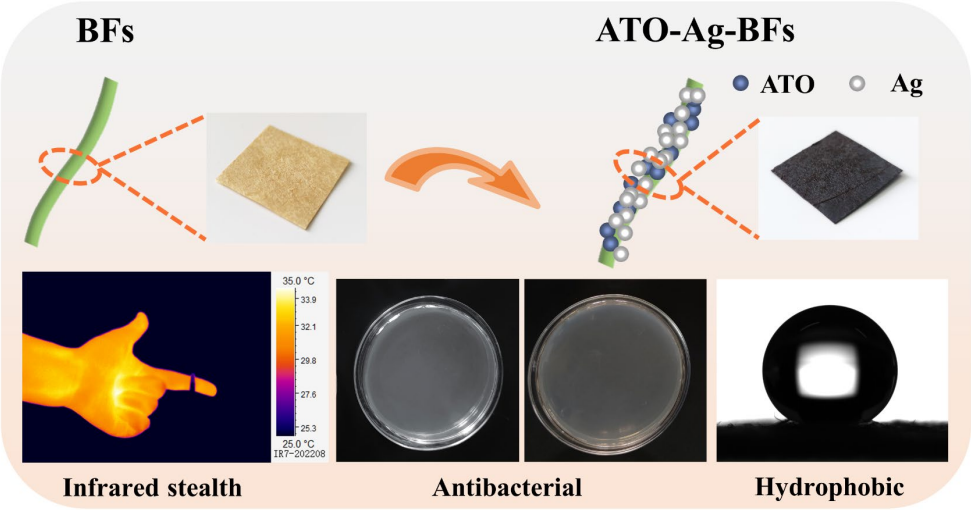

An antimony doped tin oxide/silver/bamboo fibers (ATO-Ag-BFs) composite fabrics were developed with multi-functional properties including infrared protection, antibacterial and hydrophobic properties.